Brittle creep, damage and time to failure in rocks

David Amitrano, A. Helmstetter

Brittle creep, damage and time-to-failure in rocks

David Amitrano[1] and Agnès Helmstetter[2]

[1], LIRIGM-LGIT, Grenoble University, France

[2], LGIT, Grenoble University, France

Abstract. We propose a numerical model based on static fatigue laws in order to model the time-dependent damage and deformation of rocks under creep. An empirical relation between time-to-failure and applied stress is used to simulate the behavior of each element of our finite element model. We first review available data on creep experiments, in order to study how the material properties and the loading conditions control the failure time. The main parameter that controls the failure time is the applied stress. Two commonly used models, an exponential $t_f \sim \exp(-b\sigma/\sigma_0)$ and a power law function $t_f \sim \sigma/\sigma_0{}^{b'}$ fit the data as well. These time-to-failure laws are used at the scale of each element to simulate its damage as a function of its stress history. An element is damaged by decreasing its young modulus, to simulate the effect of increasing crack density at smaller scales. Elastic interactions between elements and heterogeneity of the mechanical properties lead to the emergence of a complex macroscopic behavior, which is richer than the elementary one. In particular, we observe primary and tertiary creep regimes associated respectively with a power-law decay and increase of the rate of strain, damage event and energy release. Our model produces a power-law distribution of damage event sizes, with an average size that increases with time as a power-law until macroscopic failure. Damage localization emerges at the transition between primary and tertiary creep, when damage rate starts accelerating. The final state of the simulation shows highly damaged bands, similar to shear bands observed in laboratory experiments. The thickness and the orientation of these bands depend on the applied stress. This model thus reproduces many properties of rock creep, which were previously not modeled simultaneously.

1. Introduction

Rocks subjected to a constant stress, i.e., in creep conditions, deform at a strain rate variable with time. The study of the fracture and deformation of rocks under creep is useful to better understand the behavior of geological structures, such as volcanoes, landslides, rock massifs, and faults, which are subjected to a long-term loading.

Three regimes are usually observed during creep experiments: primary creep (decreasing strain rate), secondary creep (constant strain rate), and, for large enough stress, tertiary creep (increasing strain rate), ending by failure [*Scholz*, 1968b; *Lockner*, 1993a; *Boukharov et al.*, 1995].

During primary creep, the strain rate usually decreases as a power-law of the time since the stress change. This experimental law was first observed for metals [*Andrade*, 1910], and then for many other materials, such as rocks [*Lockner*, 1993b] and glass/polyester composite materials [*Nechad et al.*, 2005a]. Andrade's law, which describes the strain rate following a stress step, is similar to Omori's law [*Omori*, 1894] for earthquakes, which characterizes the power-law decay of aftershock rate as a function of the time after the mainshock. This similarity led several authors to suggest that aftershocks are triggered by the coseismic static (permanent) stress increase induced by the mainshock, and to apply brittle creep laws to model the temporal behavior of seismicity [e.g. *Scholz*, 1968b; *Das and Scholz*, 1981; *Shaw*, 1993; *Main*, 2000; *Perfettini and Avouac*, 2004].

The strain rate during secondary creep is nearly constant, and strongly depends on the applied stress. *Lockner* [1993b] and *Ngwenya et al.* [2001] found that both an exponential law and a power law provide a good fit to experimental measurements of the strain rate during secondary creep, for different values of the applied stress. The secondary creep regime is not always clearly observed. In some cases, there is rather a cross-over between decaying primary creep and accelerating tertiary creep than a purely stationary regime [*Lockner*, 1993b].

Creep experiments on heterogeneous materials have revealed a power-law acceleration of strain rate [*Voight*, 1988b, 1989; *Guarino et al.*, 2002; *Nechad et al.*, 2005a, b] and acoustic emission rate [*Guarino et al.*, 1999, 2002] during tertiary creep. Similar power-law accelerations of either strain rate or seismic event rate before rupture have also been observed for natural structures such as landslides [*Saito and Uezawa*, 1961; *Saito*, 1965, 1969; *Petley et al.*, 2002], volcanoes [*Voight*, 1988a] or cliff collapse [*Amitrano et al.*, 2005].

Main [2000] suggested that the precursory acceleration of seismicity sometimes observed before large earthquakes is similar to the acceleration of deformation and damage during tertiary creep. However, for earthquakes, this precursory acceleration of seismicity is not systematic, but is only significant when averaging over a large number of sequences, and can be explained by the properties of earthquake triggering [*Helmstetter et al.*, 2003].

Experimental observations, such as an increase of dilatancy and hydraulic permeability, a decrease of elastic modulus, and the recording of acoustic emission, attest that crack propagation is acting during creep [*Scholz*, 1972; *Lockner and Byerlee*, 1980; *Kranz et al.*, 1982; *Hirata et al.*, 1987; *Atkinson*, 1991; *Lockner*, 1993b; *Baud and Meredith*, 1997; *Kawada and Nagahama*, 2004]. Different approaches are used to model the time-dependent deformation of rocks. Constitutive laws, based on laboratory experiments, provide a relation between strain, stress, and strain

0148-0227/06/$9.00

rate [*Voight*, 1988b; *Lockner*, 1998; *Shcherbakov and Turcotte*, 2003]. These models reproduce the behavior of different types of rocks under different loading conditions (creep, constant stress rate or strain rate). For instance, the constitutive law derived by *Lockner* [1998] reproduces Andrade's law in the primary creep regime, as well as a power-law acceleration of the strain rate during tertiary creep.

Other approaches to model brittle creep often involve a network of a large number of elements, which interact by sharing the applied load equally among all intact elements (fiber bundle models) [*Coleman*, 1956, 1958; *Vujosevic and Krajcinovic*, 1997; *Ciliberto et al.*, 2001; *Politi et al.*, 1995; *Hidalgo et al.*, 2002; *Turcotte et al.*, 2003; *Pradhan and Chakrabarti*, 2003; *Nechad et al.*, 2005a, b]. Each element is supposed to represent the mesoscale, much larger than the size of one crack, and much smaller than the system size. These models only provide the temporal evolution of strain and damage during creep, but cannot model its spatial distribution (localization before failure), or the size distribution of damage events. A few models use elastic long-range interactions [*Sornette and Vanneste*, 1994], and can thus model the progressive nucleation, growth and fusion between microcracks, leading to a fractal network of micro-cracks [*Sornette and Vanneste*, 1994]. Each element has either an elastic-brittle [*Coleman*, 1956, 1958; *Vujosevic and Krajcinovic*, 1997; *Ciliberto et al.*, 2001; *Politi et al.*, 1995; *Turcotte et al.*, 2003; *Pradhan and Chakrabarti*, 2003; *Sornette and Vanneste*, 1994] or viscous-brittle rheology [*Hidalgo et al.*, 2002; *Nechad et al.*, 2005a, b]. The strength of each element depends on time, and on the stress or strain on this element. Complexity is introduced in these models using (i) thermal noise, by introducing a failure probability per time unit that depends on the stress or strain on each element, or by adding random fluctuations to the stress [*Coleman*, 1956, 1958; *Vujosevic and Krajcinovic*, 1997; *Ciliberto et al.*, 2001; *Politi et al.*, 1995; *Turcotte et al.*, 2003; *Pradhan and Chakrabarti*, 2003], and/or (ii) quenched disorder, i.e., frozen heterogeneity of the mechanical properties of each element [*Sornette and Vanneste*, 1994; *Ciliberto et al.*, 2001; *Politi et al.*, 1995; *Nechad et al.*, 2005a, b].

At the microscopic scale, other studies modeled the growth of individual cracks, and the resulting macroscopic strain [e.g. *Lockner*, 1993b; *Miura et al.*, 2003]. *Lockner* [1993b] derived a law for the temporal evolution of strain based on reaction rate theory. His model recovers Andrade's law for the primary creep regime, and reproduces empirical laws between strain rate and stress during secondary creep. But this model cannot produce an accelerating tertiary creep because it does not include crack interactions.

To our knowledge, no model has attempted to model at the same time all properties of rocks under creep, including the temporal evolution of strain and damage during primary, secondary and tertiary creep, the progressive damage localization before failure, as well as the power-law distribution of acoustic event sizes.

In this paper, we develop a model for the time-dependent deformation and damage of rocks. Our model reproduces both the temporal evolution of damage and its spatial distribution. It is a 2D finite-element model with an elastic-brittle rheology. The damage parameter of each element, which represents the density of fractures in this element, evolves as a function of the stress history. It can be compared with acoustic emission recorded during creep experiments. We first review experimental results on the influence of the loading conditions (stress, fluid pressure, temperature) on the time to failure. We compare two models for the relation between time to failure and applied stress: exponential and power law functions of the applied stress. These relations are then used as an input for our numerical model, in order to characterize the damage of each element as a function of the load applied to this element.

Our model is an extension of the time-independent model introduced by *Amitrano et al.* [1999] and *Amitrano* [2003]. In this previous model, an element is damaged (its Young's modulus decreased) only when its stress reaches a given threshold. The macroscopic behavior of the system is characterized by a power-law distribution of avalanches, damage localization, and a transition from brittle to ductile behavior as a function of the confining pressure or of the friction coefficient. These properties are not included in the elementary behavior, but emerge from the interaction between elements, showing that deformation process is a complex phenomenon [*Amitrano*, 2004].

This previous model was however unable to explain the delayed failure of rocks under a stress smaller than its instantaneous strength. The introduction of a time-to-failure law in our new model enable us to reproduce the time evolution of the strain and acoustic emission observed experimentally (primary, secondary, and tertiary creep regimes), as well as the progressive damage localization before failure. Analytical results are obtained for a simplified version of our model, which reveal the main mechanisms that control the temporal evolution of strain and damage. Table 1 summarizes the main notations used in this paper.

2. Time-to-failure of rocks

When subjected to a constant stress smaller than the instantaneous strength, rocks deform and eventually fail, after a time delay that depends on the applied stress. In this section, we first describe theoretical and empirical models for the relation between failure time and applied stress. We then review available experimental results to test which model best fits the data.

2.1. Delayed failure and sub-critical crack growth

The subcritical growth of microcracks, also called static fatigue, is suggested to be the main mechanism responsible for the brittle creep of rocks, and for delayed failure [*Scholz*, 1972; *Lockner*, 1993b]. Laboratory experiments have monitored the subcritical growth of cracks, for a stress intensity factor K smaller than the critical intensity factor K_c which corresponds to instantaneous failure [see *Atkinson*, 1991, for a review]. Macroscopic failure is thus assumed to occur when the crack density and/or the crack velocity reaches a threshold.

Subcritical cracking can be explained by the reaction rate theory, considering that atomic bonds may break due to thermal fluctuations. This is enhanced by the stress concentration at the crack tips [see *Atkinson*, 1991, p 128-130, for a more detailed presentation]. Therefore the subcritical crack growth depends on ambient conditions and is enhanced when temperature is increased. Considering an exponential dependence between stress and activation energy, *Wiederhorn and Bolz* [1970] proposed an empirical law for glasses that describe well a wide range of experimental observations, including for rocks [*Atkinson*, 1984].

$$V = V_0 \exp\left(\frac{-W_0 + BK}{RT}\right) \tag{1}$$

where V is the crack propagation velocity, R is the gas constant, T the temperature, W_0 the activation energy, K the stress intensity factor, B and V_0 are constants. The parameters W_0, B and V_0 depend on the material properties and on the environmental conditions. The stress intensity factor K is proportional to $\sigma\sqrt{L}$, where L is the crack length, with an additional factor which depends on the crack shape. Considering a different stress dependence of the chemical reactions involved in static fatigue, a power law relation between crack

velocity and intensity factor has been proposed by *Charles* [1958] for glass and applied to rocks [e.g. *Atkinson*, 1984]:

$$V = V_0 \left(\frac{K}{K_c}\right)^q \exp\left(\frac{-W_0}{RT}\right) . \quad (2)$$

The exponent q is usually large, i.e, $q \approx 20$, so that the power law form (2) is almost indistinguishable from the exponential law (1).

The relationships (1) and (2) describe the propagation of single cracks. They can be used to infer the time-to-failure of a sample as a function of the loading conditions.

2.2. Models for time to failure

The time-to-failure can be deduced from relations (1) or (2), using the definition $K \sim \sigma\sqrt{L}$, and assuming that failure occurs when the crack velocity diverges or when it reaches a given threshold [*Wiederhorn and Bolz*, 1970; *Das and Scholz*, 1981; *Shaw*, 1993]. This last hypothesis is in agreement with the experimental observations of *Baud and Meredith* [1997], who observed that, for different stress values, the amount of acoustic emission, the permeability and the total deformation at failure vary by less than 20%, while the time-to-failure varies by several orders of magnitude. For an exponential relation (1), the average time-to-failure is related to the applied stress by [*Wiederhorn and Bolz*, 1970; *Das and Scholz*, 1981]

$$t_f = t_0 \exp\left(-b\frac{\sigma}{\sigma_0}\right) \quad (3)$$

where σ is the major stress and σ_0 is the instantaneous strength (i.e., $t_f = 0$ for $\sigma > \sigma_0$).

Assuming a power-law relation between V and K given by (2) , the time to failure is [*Charles*, 1958]

$$t_f = t_0' \left(\frac{\sigma}{\sigma_0}\right)^{-b'} \quad (4)$$

with an exponent $b' = q - 2$. The relation (4) has also been observed experimentally [*Cruden*, 1974]. In both cases, exponential (3) and power law (4) models, the constants t_0 or t_0', b or b', and σ_0 depend on rock properties and ambient conditions [see *Scholz*, 1972, and references therein].

Although not observed in the laboratory because of time constraints there should be a lower cut-off for subcritical crack growth corresponding to the stress level under which corrosion blunts the crack tips [*Cook*, 1986; *Freiman*, 1984]. As no experimental values are available for estimating this cut-off, we have not included this phenomenon in our model.

2.3. Review of experimental data

The time-to-failure of rocks under creep is suggested empirically to decrease with the stress either exponentially or as a power law [*Scholz*, 1968b, 1972; *Cruden*, 1974; *Kranz*, 1980; *Kranz et al.*, 1982; *Boukharov et al.*, 1995; *Baud and Meredith*, 1997; *Lockner*, 1998; *Di Giovambattista and Tyupkin*, 2001; *Masuda*, 2001; *Kawada and Nagahama*, 2004]. The same relations are found for other heterogeneous media such as concrete, glass fiber composite, plexiglass or chipboard wood panels [e.g. *Guarino et al.*, 1999; *Ciliberto et al.*, 2001; *Purnell et al.*, 2001; *Guarino et al.*, 2002].

Hereafter we analyze data published in the literature [*Scholz*, 1972; *Kranz*, 1980; *Kranz et al.*, 1982; *Baud and Meredith*, 1997; *Masuda*, 2001] in order to quantify the impact of the loading conditions (stress, confining pressure, temperature, saturation) on the time-to-failure of samples loaded under creep conditions (i.e. constant stress below the instantaneous strength σ_0). We first test which time-to-failure relation, exponential (3) or power-law (4), better explains the data. In order to compare uniaxial ($\sigma_1 > \sigma_2 = \sigma_3 = 0$) and triaxial ($\sigma_1 > \sigma_2 = \sigma_3 \neq 0$) creep tests, the applied major stress σ has been normalized by the instantaneous strength σ_0 (maximum value of the applied stress for short times, i.e., few minutes, failure). For each data set, we perform a linear least-squares fit for the exponential law $\log(t_f) = -b\sigma/\sigma_0 + \log(t_0)$ and for the power law model $\log(t_f) = -b' \log(\sigma/\sigma_0) + \log(t_0')$. For each fit, we estimate the regression coefficients $\log(t_0)$ or $\log(t_0')$, and b or b', and the linear correlation coefficient r between $\log(t_f)$ and σ/σ_0 (exponential fit (3)) or $\log(\sigma/\sigma_0)$ (power-law relation (4)). The results of these fits are presented in Table 2 and in Figure 1.

We find that, for all data sets, the exponential and power law fits are equivalent in terms of correlation coefficient. This small difference between the exponential and power-law fits can be attributed to both the high exponent values (b and b' ranging from 20 to 140) and to the narrow range of normalized stress (σ/σ_0 ranging from 0.7 to 0.98). Under these conditions the two laws cannot be distinguished. For each law, the exponent b or b' indicates the stress dependence of the time to failure. A given variation of the applied stress has a stronger impact on the time-to-failure for a higher value of b or b'.

Most creep experiments are performed at room conditions (no confining pressure, temperature near 20°C, water saturation corresponding to the ambient air), but a few authors have investigated the impact of environmental conditions on the time to failure. They found that the time-to-failure increases when increasing the confining pressure [*Kranz*, 1980; *Baud and Meredith*, 1997; *Lockner*, 1998], decreasing the temperature [*Scholz*, 1972; *Kranz et al.*, 1982] or the water saturation [*Scholz*, 1972; *Kranz et al.*, 1982; *Masuda*, 2001]. *Scholz* [1972] observed experimentally the relation (3) for single-crystal quartz samples broken in uniaxial compression. He found that the characteristic time t_0 in (3) decreases with the water concentration as $t_0 \sim C_{H_2O}{}^{-\alpha}$, and decreases with the temperature as $t_0 \sim \exp(W_0/RT)$. These results suggest that static fatigue of quartz can be explained by corrosion microcracking. The exponent b in (3) did not show any significant change with the water concentration or the temperature, though not enough experiments were performed to verify the independence of b and T. The b-exponent was only sensitive to the microstructure, with a larger b-value for samples loaded along the c-axis than for the a-axis (see Table 1).

The triaxial tests of *Kranz* [1980] suggest an increase of b and t_0 with the confining pressure σ_3. But the number of samples in these experiments is very small, and more experiments should be done to confirm this result. This can be related to the impact of the confining pressure which tends to decrease the stress intensity factor K. Another explanation is that cracks close when increasing the confining pressure, so that part of the mechanical energy is consumed by friction. The experiments of *Kranz et al.* [1982] give slightly larger values of b and t_0 for the dry sample than for the wet sample. *Kranz et al.* [1982] also found a decrease of b and t_0 with the temperature, as expected for stress-corrosion cracking (1).

In this paper, we will consider only the effect of stress on the time-to-failure, using expressions (3) or (4). The influence of other parameters, such as temperature, water saturation and confining pressure, can be accounted for by changing the parameters t_0, b and b'. For geological objects, such as volcanoes, landslides or faults, the pressure, the temperature and the water content may be very variable, e.g., as a function of depth, or change with time. We thus need to account for this variability when modeling the deformation and failure of geological objects, by changing the parameters of the time-to-failure law. For instance, it is well established that landslides movement accelerates in wet condition [e.g. *Caine*, 1980]. Fluids decrease the effective normal stress, thus reducing the shear strength of the rock mass. But fluids also increase the strain rate and decrease the time to failure due to chemical reactions, as shown in the creep experiments of *Scholz* [1972].

3. Description of the numerical model

The model we develop here is based on the progressive damage model of *Amitrano et al.* [1999]. This model simulates a macroscopic behavior that ranges from brittle to ductile, associated to localized or diffuse damage respectively. This model also describes the evolution of acoustic emission (size and location of rupture avalanches) during the progressive damage process. It allows us to simulate a large range of observations, from the laboratory scale [*Amitrano*, 2003] to the Earth's crust scale [*Sue et al.*, 2002; *Amitrano*, 2004], but is restricted to the time-independent behavior of rocks, i.e., short times. We first summarize the main features of this model, and then focus on incorporating time dependence in the model.

3.1. Time-independent model

The system is discretized using a 2D finite element method with plane strain assumption. The model is based on progressive isotropic elastic damage. When the stress on an element exceeds a damage threshold, its elastic modulus E_i is modified according to

$$E_i(n+1) = E_i(n)(1 - D_0)\,, \tag{5}$$

where D_0 is a constant damage parameter ($D_0 = 0.1$ in our simulation). After n damage events, the effective modulus $E_i(n)$ of element i is given by

$$E_i(n) = (1 - D_0)^n\, E_{i,0} = (1 - D_i(n))\, E_{i,0}\,, \tag{6}$$

where $E_{i,0}$ is the initial Young's modulus, and the damage parameter is given by $D_i(n) = 1 - (1 - D_0)^n$. This relation (6) describes the damage of a volume much larger than the defect size (i.e., cracks). The damage parameter $D_i(n)$ is related to crack density [see *Kemeny and Cook*, 1986, for a review]. Because of elastic interactions, stress redistribution around a damaged element can induce an avalanche of damage events. The total number of damaged elements during a single loading step is the avalanche size, which is comparable to the size of an acoustic emission in laboratory experiments.

The Mohr-Coulomb criterion is used as a damage threshold. The instantaneous strength σ_0 is determined for each element by

$$\sigma_0 = \sigma_3\, \frac{1 + \sin\phi}{1 - \sin\phi} + \frac{2C\cos\phi}{1 - \sin\phi}\,, \tag{7}$$

where C is the internal cohesion, ϕ the internal friction angle, and σ_3 is the minor stress on the element. We choose this criterion because of its simplicity, and because it allows to check independently the influence of each parameter (C, ϕ, and normal stress σ_3). Without time dependence, an avalanche occurs only when the stress is increased, by increasing the vertical displacement of the upper model boundary.

In the absence of heterogeneity, the behavior of the model is entirely homogenous, i.e., no damage localization occurs, and the local behavior is replicated at the macroscopic scale. It is necessary to introduce heterogeneity to obtain a macroscopic behavior different from those of the elements. In order to model material heterogeneity, the cohesion of each element C is drawn randomly from a uniform distribution in the range $C_1 - C_2$ (25-50 MPa). Due to this heterogeneity, the stress on each element is different from the macroscopic stress imposed at the upper boundary of the model. The other mechanical parameters are fixed (Young's modulus E=50 GPa, Poisson coefficient ν=0.25, internal friction coefficient $\tan\phi$=0.5).

According to this mesoscale approach, the model neglects the details of microcracking processes at small scale. It is well established that at the grain size the deformation is dominated by tensile cracks orientated parallel to σ_1, particularly visible through the phenomenon of dilatancy [*Scholz*, 1968a; *Lockner et al.*, 1991; *Moore and Lockner*, 1995; *Vermilye and Scholz*, 1998; *Katz and Reches*, 2004]. Small scale tensile cracks are simulated in our model by decreasing the Young's modulus of an element, to simulate the effect of increasing micro-crack density. This mesoscale approach may be used as an alternative [*Amitrano*, 2006] to the microscopic approach, dedicated to the study of fracture propagation [e.g. *Lockner and Madden*, 1991a, b; *Reches and Lockner*, 1994], and to the macroscopic approach based on constitutive laws [e.g. *Lockner*, 1998; *Kawada and Nagahama*, 2004]. This allow us to investigate the collective behavior of interacting elements and the emergence of a complex macroscopic behaviour.

3.2. Time-dependent model

In order to simulate the time-dependent behavior of rocks, we introduce a time-to-failure law to model the failure by static fatigue of each element i when subjected to a constant stress σ_i (major stress on this element) smaller than its instantaneous strength $\sigma_{0,i}$. We use either the exponential (3) or the power-law (4) relation between the time-to-failure of each element and its normalized stress $\sigma_i/\sigma_{0,i}$. The system is loaded by imposing a constant stress σ on its upper boundary. The simulation stops when the macroscopic strain reaches a threshold ϵ_c, as observed experimentally [e.g. *Baud and Meredith*, 1997; *Kranz et al.*, 1982]. We use $\epsilon_c = 0.03$.

An element fails either when the time t is equal to its failure time t_i, or, during an avalanche, when the stress σ_i on this element reaches the rupture criterion $\sigma_{0,i}$ (7). The damage parameter, the stress, the strength, and the failure times of all elements are updated after each failure.

We characterize the state of each element by its failure time t_i, and by a parameter p_i that represents the proportion of consumed lifetime. This allows us to estimate the remaining time-to-failure for an element taking into account its stress history. The parameter t_i gives the failure time of this element, measured from the beginning of the simulation, in the absence of interactions between elements. Initially, the failure time of the i^{th} element is given by the time-to-failure law, i.e., $t_i(0) = t_f(\sigma_i, \sigma_{0,i})$, and the proportion of consumed lifetime is $p_i(0) = 0$. The time-to-failure $t_f(\sigma_i, \sigma_{0,i})$ is given either by the exponential (3) or the power-law (4) relation.

After each damage event, we update the damage, the stress, and the strength of each element, and then its consumed lifetime and its failure time. If element i was not broken during the first event at time $t(1)$, the proportion of consumed lifetime is simply given by $p_i(1) = t_1/t_i(0)$. For all elements damaged during the avalanche, the proportion of consumed lifetime is reset to zero $p_i(1) = 0$. The new failure time of each element, measured from the origine $t = 0$, is then given by

$$t_i(1) = t_1 + t_f(\sigma_i, \sigma_{0,i})\,(1 - p_i(1))\,. \tag{8}$$

After the n^{th} avalanche, at time $t(n)$, the proportion of consumed lifetime for elements that are not damaged during the n^{th} avalanche is updated according to

$$p_i(n) = p_i(n-1) + \frac{t(n) - t(n-1)}{t_i(n-1) - t(n-1)}\,. \tag{9}$$

For all elements damaged during the avalanche, the proportion of consumed lifetime is reset to zero:

$$p_i(n) = 0 \tag{10}$$

Extrapolating (8) to $n > 1$, the failure time after the n^{th} avalanche is given by

$$t_i(n) = t(n) + t_f(\sigma_i, \sigma_{0,i})\,(1 - p_i(n))\,, \qquad (11)$$

This approach (11) and (9) was experimentally tested to estimate the time-to-failure of samples subjected to a stress increase [*Guarino et al.*, 1999] and gave satisfactory results. In expression (11), the time-to-failure is independent of damage. In order to take into account experimental observations showing that the time-to-failure decreases linearly with the amount of damage [e.g. *Ray et al.*, 1999], we introduce the damage factor $(1 - D_i(n))$ in the previous expression (11)

$$t_i(n) = t_n + t_f(\sigma_i, \sigma_{0,i})\,(1 - p_i(n))\,(1 - D_i(n))\,, \quad (12)$$

where $D_i(n)$ defined by (6) is the total damage parameter of element i after n damage events.

We have tested both laws (11) and (12) in our numerical simulations. Both laws give similar results in the primary creep regime, but the introduction of the damage parameter in (12) is necessary to obtain a power-law acceleration in the tertiary creep regime. In comparison, the choice of the exponential (3) or the power-law (4) time-to-failure relation has little influence in the simulations.

4. Results of the numerical simulations

4.1. Temporal evolution of strain and damage

Figure 2 shows the typical evolution of strain, number of damage events, and energy release up to failure, for two simulations with σ/σ_0=0.80 and b=40 or b'=40. We obtain similar results for the exponential (3) and power-law (4) time-to-failure laws. For all values of σ and b or b', and when decreasing the time-to-failure of each element with damage according to (12), we observe both primary and tertiary creep regimes, characterized respectively by decreasing and increasing strain rate. We observe a similar behavior for the number of damage events and for the cumulative energy release. The secondary creep regime does not appear in the simulations (no stationary regime), but may be rather defined as the transition between primary and tertiary creep corresponding to the minima of the strain rate. Figure 3 shows the rate of damage events, the strain rate, and the rate of energy release as a function of time (normalized by the failure time t_c of each simulation), for different values of the applied stress.

During primary creep, both the strain rate $\dot\epsilon(t)$, the rate of damage events $\dot n(t)$ and the energy release rate $\dot W(t)$ decay with time approximately as a power-law, equivalent to Omori's law [*Omori*, 1894] for earthquakes, and known as Andrade's law [*Andrade*, 1910] for the strain rate in creep experiments:

$$\dot\epsilon(t) \;\sim\; \frac{1}{t^{p_\epsilon}} \qquad (13)$$

$$\dot n(t) \;\sim\; \frac{1}{t^{p_n}} \qquad (14)$$

$$\dot W(t) \;\sim\; \frac{1}{t^{p_W}} \qquad (15)$$

with both exponents p_ϵ, p_n and p_W, slightly smaller than 1 (see Figure 3). Experimentally, the exponent p_n was found equal to 0.5 ± 0.25 by *Scholz* [1972], for quartz samples. *Andrade* [1910] suggested an exponent $p_\epsilon = 2/3$ for metals. This value has been reproduced by numerical simulations based on interacting dislocations [*Miguel et al.*, 2002]. *Nechad et al.* [2005a] reported average values $p_\epsilon = 0.86$ and $p_n = 0.63$, estimated for 15 samples of fiberglass composites loaded under constant tension.

After the primary creep regime, the strain rate and the damage rate increase due to interactions between elements and due to increasing damage. However, this tertiary creep regime is observed only when using expression (12) for the failure time of each element as a function of damage, stress and strength. Otherwise, if the time-to-failure does not decrease with damage, the simulation reaches a constant stationary regime at large times, characterized by a constant strain rate and event rate. These results are understood qualitatively by the analytical study presented in section 5.

In the model, when using expression (12) for the failure time, we observe a power-law acceleration of the strain rate $\dot\epsilon$, of the rate of damage events $\dot n$, and of the energy release rate $\dot W$

$$\dot\epsilon(t) \;\sim\; \frac{1}{(t_c - t)^{p'_\epsilon}} \qquad (16)$$

$$\dot n(t) \;\sim\; \frac{1}{(t_c - t)^{p'_n}} \qquad (17)$$

$$\dot W(t) \;\sim\; \frac{1}{(t_c - t)^{p'_W}} \qquad (18)$$

The critical time t_c in (16), (17) and (18) is the time of the end of the simulation, when the strain ϵ reaches the threshold ϵ_c. The exponent p'_n is smaller than 1, typically $p'_n \approx 0.8$. The strain rate and energy release accelerate faster than the rate of damage events, with exponents $p'_W \approx p'_\epsilon \approx 1.3$. These exponents do not depend on the applied stress (except for very large stress $\sigma/\sigma_0 = 0.95$), and on b or b' (as long as $b \gg 1$ or $b' \gg 1$ as observed experimentally).

The macroscopic failure time t_c has the same dependence with the applied stress as the time-to-failure of each element (given by (3) or (4)). We find at the macroscopic level the same law as we used as input at the scale of each element.

The curves in Figure 3 show that, when normalizing time by t_c, the curves of $\dot\epsilon(t)$, $\dot n(t)$ or $\dot W(t)$ for different values of the applied stress are almost superposed. In particular, the transition time t_m between primary and tertiary creep (given by the minima of $\dot\epsilon(t)$) is about half the failure time, i.e, $t_m \approx t_c/2$. A similar result was previously obtained experimentally by *Nechad et al.* [2005a] for creep tests on glass-fiber composites, who observed $t_m \approx 2/3\,t_c$, and was also observed in a creep model of visco-elastic fibers [*Nechad et al.*, 2005a].

4.2. Distribution of event sizes

Figure 4 shows the energy distribution $P(\Delta W, t)$ and its evolution with time. For small stress $\sigma/\sigma_0 = 0.25$, the instantaneous energy distribution is very narrow, with an average value and a standard deviation increasing with time. When integrating over the complete simulation, the event size distribution is close to a power-law $P(\Delta W) \sim \Delta W^{-1-\beta}$, with $\beta \approx 1$, larger than the value $\beta = 2/3$ commonly observed for the distribution of earthquakes seismic moments [*Kagan*, 1999]. For larger stresses, the event size distribution is almost independent of time. There is only a small increase of the fraction of large events before t_c. However, the absence of a clear acceleration for large stress may be due to the small number of events observed very close to failure. Figure 5 shows the evolution of the median energy of damage events as a function of the time before failure, $t - t_c$. For all values of the stress, the typical energy increases as a power-law before failure, with an exponent around 0.3. We observed similar results if we consider the average energy instead of the median, with larger fluctuations. Figure 6 shows the cumulative energy distribution, for all events in the simulation, for different stress values. For small stress $\sigma/\sigma_0 < 0.9$, $P(\Delta W)$ is a power-law for small energies with an exponential fall-off, which progressively vanishes when

stress increases. For larger stress, $P(\Delta W)$ shows a small excess of large events relative to the power-law distribution observed for small ΔW.

4.3. Spatial distribution of damage

Figure 7 shows the final damage state $D_i(n)$ defined by (6), for different values of the applied stress. We see that damage becomes more localized as stress increases. The thickness of the bands decreases with the applied stress. For $\sigma/\sigma_0 = 0.5$, it is about the size of 10 elements (for a system of 32 by 16 elements). For larger stress $\sigma/\sigma_0 = 0.95$, the width of the damage bands is only one element. The orientation of the shear bands relative to the major stress also depends on the applied stress, from $\approx 45^o$ for small stress $\sigma/\sigma_0 = 0.5$, down to $\approx 30^o$ for larger stresses. For large stress (thin bands), the orientation and the width of the shear bands are constrained by the meshing structure.

In order to quantify the spatial structure of the damage, we have calculated the directional spatial correlogram (DSC) of the total damage $D_i(n) = 1 - E_i(n)/E_{i,0}$ (where n is the number of damage events of element i). For a given direction $\vec{d}$, the DSC is calculated as the autocorrelation function along this direction, i.e., the correlation between the damage value observed at point x and at point x' separated by a distance λ along direction $\vec{d}$ (at an angle α relative to the loading direction). The correlation is calculated as the covariance between $D(\vec{x})$ and $D(\vec{x} + \lambda\vec{d})$ divided by the variance of $D(\vec{x})$

$$\begin{aligned} DSC(\alpha,\lambda) &= \mathrm{r}\left(D(\vec{x}),\, D(\vec{x}+\lambda\vec{d})\right) \\ &= \frac{\mathrm{var}\left(D(\vec{x}),\, D(\vec{x}+\lambda\vec{d})\right)}{\mathrm{var}\left(D(\vec{x})\right)}\,. \end{aligned} \tag{19}$$

We have calculated the DSC as a function of the distance λ for all values of α between 0 and 180°, with a step of 5°. This analysis reveals the spatial correlation of the damage and its anisotropy.

The direction of the bands is characterized by a long range correlation, and the perpendicular direction by a correlation length equivalent to the band thickness.

For each direction α, the DSC is maximum for short distances, and then decreases more or less continuously for increasing λ, as shown in Figure 8, for the directions parallel and perpendicular to the bands. Figure 8 shows that the correlation length is almost zero at short times, and then increases with time. For large distances (larger than the band width), $DSC(\alpha,\lambda)$ is maximum in the direction of the damage bands.

In order to quantify the damage anisotropy, we have calculated the difference between the correlogram in the direction α, and its perpendicular direction, integrated over all distances λ.

$$A(\alpha) = \int_0^{\lambda_{\max}} \left[DSC(\alpha,\lambda) - DSC(\alpha+\pi/2,\lambda)\right] d\lambda\,. \tag{20}$$

If the damage is anisotropic, the coefficient A is large in the direction of the damage band, as the difference between DSC in this direction and the perpendicular is maximal.

We can identify in Figure 9 the band direction $\alpha_{\mathrm{band}} = 30^o$ for which $A(\alpha)$ is maximum. Figure 9 shows $A(\alpha)$ for different times during the simulation. Each curve corresponds to a constant number $n = 800$ of events. Damage is initially isotropic ($A(\alpha)$ is near zero and is independent of α), and becomes anisotropic during tertiary creep. The time $t/t_c \approx 0.5$ when anisotropy appears coincides with the transition between primary and tertiary creep, when strain rate and damage rate start increasing.

5. Analytical study

In this section, analytical results are obtained for a simplified version of our model, which reveal the main mechanisms that control the temporal evolution of strain, energy and damage.

5.1. Relation between damage and strain

Considering a uniaxial stress state which can be described by the scalar value of the major stress σ (a similar analysis can be performed for a tensorial description of the stress state), we can estimate the strain variation induced by a single damage event. We can then derive an approximate analytical relation between the strain rate $\dot{\epsilon}(t)$ and the rate of damage events $\dot{n}(t)$ by assuming that

- the average number s of elements which breaks during each avalanche does not change with time (this is not always the case in the numerical simulations);
- before the avalanche, the Young's modulus of an element i that breaks is equal to the average Young's modulus of the system $E_i =< E >= E$;
- all elements have the same major stress, equal to the applied load σ, and the same axial deformation $\epsilon = E\sigma$.

Under these assumptions, the new Young's modulus of a damaged element after an avalanche is $E'_i = E_i\,(1 - D_0) = E\,(1 - D_0)$. The new average Young's modulus E' of the system of N elements after an avalanche of size s is

$$E' = \frac{E\,(N-s)}{N} + \frac{E\,s\,(1-D_0)}{N} = E\,\frac{N - s\,D_0}{N}\,. \tag{21}$$

The deformation of the system after the avalanche is

$$\epsilon' = \frac{\sigma}{E'} = \frac{\sigma}{E}\,\frac{N}{N - s\,D_0} = \epsilon\,\frac{sN}{N - s\,D_0}\,. \tag{22}$$

We can write the strain rate $\dot{\epsilon}(t)$ as

$$\dot{\epsilon}(t) = \frac{\epsilon' - \epsilon}{\Delta t} = \frac{\epsilon}{\Delta t}\,\frac{D_0}{N - s\,D_0} \tag{23}$$

where Δt is the inter-event time at time t.

We can now compute the rate of damage events at time t as $\dot{n}(t) = 1/\Delta t$. Using (23), we get the relation between strain rate and damage rate:

$$\dot{n}(t) = \frac{\dot{\epsilon}(t)}{\epsilon(t)}\,\frac{N - s\,D_0}{s\,D_0} \tag{24}$$

5.2. Relation between strain and released energy

The energy release induced by an avalanche of size s is given by the change in elastic energy (assuming a constant uniform stress σ on all elements)

$$\Delta W = \frac{1}{2}\Delta(\sigma\,\epsilon) = \frac{1}{2}\sigma\,\Delta\epsilon\,. \tag{25}$$

Using expression (22), we obtain

$$\Delta W = \frac{\sigma\,\epsilon}{2}\,\frac{s\,D_0}{N - s\,D_0}\,. \tag{26}$$

The fact that energy release is proportional to strain explains why the exponents for strain rate and energy rate are very similar in our simulations, both during primary and tertiary creep. Differences between them can be related to the

assumption of constant stress conditions, which is verified only on average. Note that both strain change and energy release increase as the Young's modulus E decreases (i.e., as damage increases). The relation between the energy release rate and the strain rate also depends on the avalanche size s. At the beginning of the simulation, during primary creep, the mean size of damage events is essentially equal to one. The energy rate is thus proportional to strain rate, thus $p_\epsilon = p_W$. During tertiary creep, the mean avalanche size increases, thus p_W differs from p_ϵ.

5.3. Primary creep

We derive here an approximate analytical solution for the evolution of the damage rate, the strain rate, and the energy release rate during primary creep. In our model, interactions between elements are relatively weak at short times, so that the stress σ_i of each element is close to the externally applied stress σ. We consider only strength heterogeneity. The time at which each element first fails is thus close to its initial time-to-failure $t_i(0) = t_f(\sigma, \sigma_{0,i})$. Assuming that no element has ruptured more than once, the damage rate $\dot{n}$ in this regime is simply proportional to the probability distribution function (pdf) of $t_f(\sigma, \sigma_{0,i})$. The variability of $t_f(\sigma, \sigma_{0,i})$ results from the initial heterogeneity of the strength σ_0.

Therefore, the damage rate in the primary creep regime is approximately equal to:

$$\dot{n}(t) = \frac{dN}{dt_f(\sigma, \sigma_0)} = \frac{dN}{d\sigma_0} \frac{d\sigma_0}{dt_f(\sigma, \sigma_0)} \tag{27}$$

Initially, the strength σ_0 has a uniform distribution between σ_{0_1} and σ_{0_2} (values of the strength estimated using the Coulomb criterion (7) for $C = C_1$ and $C = C_2$ respectively). Therefore, the first factor in (27) is $dN/d\sigma_0 = N/(\sigma_{0_2} - \sigma_{0_1})$. The minimum time-to-failure is $t_{\min} = t_f(\sigma, \sigma_{0_1})$ (time-to-failure corresponding to the minimum value of the cohesion C_1).

If the time-to-failure has the exponential dependence with the normalized stress (3), then

$$\frac{dt_f(\sigma, \sigma_0)}{d\sigma_0} = \frac{t_0 \sigma b}{\sigma_0^2} \exp(-b\frac{\sigma}{\sigma_0}) = \frac{[t \log(t/t_0)]^2}{b\sigma}\,, \tag{28}$$

where $t = t_f(\sigma, \sigma_0)$. Expressions (27) and (28) give, for $t \geq t_{\min}$

$$\dot{n}(t) = \frac{N\sigma b}{(\sigma_{0_2} - \sigma_{0_1}) t\, [\log(t/t_0)]^2} \tag{29}$$

For $t \ll t_0$, this function (29) looks like a power law (14) with an apparent exponent $p_n \leq 1$ decreasing slowly with time.

For a power-law relation between time-to-failure and strength (4), expression (27) gives, for $t > t_{\min}$

$$\dot{n}(t) = \frac{N\sigma}{(\sigma_{0_2} - \sigma_{0_1}) b\, t_0 (t/t_0)^{1-1/b}} \tag{30}$$

For $b \gg 1$, the damage rate has a power law decay with an exponent $p_n = 1 - 1/b$ slightly smaller than 1.

In both cases (29) and (30), the effective power-law decay of the damage rate during primary creep arises from the coupling between a uniform distribution of strength and the sharp increase of the time-to-failure with strength. The large values of the damage rate at short times correspond to the elements with the smallest cohesion. The elements with a larger strength have a much longer time-to-failure. The mechanism responsible for the power-law decay of the damage rate in our model is similar to previous models of creep or of aftershocks [*Scholz*, 1968b; *Das and Scholz*, 1981; *Shaw*, 1993], except that these studies used a constant strength and a uniform distribution of stress, while the initial stress in our model is constant and only the strength is heterogeneous.

Expressions (29) and (30) are valid only when each element has ruptured only once, i.e., when time is small compared to the average time-to-failure $t_f(\sigma, \sigma_0)$. This is the case during the beginning of the primary creep regime if the strength is very heterogenous ($\sigma_{0,2} \gg \sigma_{0,1}$) and for $b \gg 1$ or $b' \gg 1$, so that a small fluctuations of σ_0 gives a large variation of $t_f(\sigma, \sigma_0)$. Also, expressions (29) and (30) are valid as long as interactions between elements are negligible, when the strain is close to its initial value. Therefore these approximate solutions are better (fit the simulations over a larger time interval) if the damage parameter is small $D_0 \ll 1$.

We can also describe the evolution of strain and energy release during primary creep by using the relation (24) between strain and damage rate derived above. For the exponential time-to-failure law (3), the solution of the differential equation (24), for the damage rate given by (29) is

$$\epsilon(t) = \frac{\sigma}{E_0} \exp\left[-a/\log(t/t_0)\right] \tag{31}$$

$$\dot{\epsilon}(t) = \frac{a\sigma}{E_0} \frac{\exp\left[-a/\log(t/t_0)\right]}{t\, [\log(t/t_0)]^2} \tag{32}$$

$$a = \left(\frac{sD_0}{N - sD_0}\right) \left(\frac{N\sigma b}{\sigma_{0_2} - \sigma_{0_1}}\right)\,. \tag{33}$$

For the power-law time-to-failure relation (4), we obtain using (24) and (30)

$$\epsilon(t) = \frac{\sigma}{E_0} \exp\left[\frac{a}{b}\left(\frac{t}{t_0}\right)^{1/b}\right] \tag{34}$$

$$\dot{\epsilon}(t) = \frac{\sigma a}{E_0 t_0 b^2} \exp\left[\frac{a}{b}\left(\frac{t}{t_0}\right)^{1/b}\right] \left(\frac{t_0}{t}\right)^{1-1/b} \tag{35}$$

In both cases, exponential (32) and power-law (35), the strain rate decays as a power-law with an exponent $p_\epsilon \approx 1$ if b or $b' \gg 1$,. The strain increases slowly with time at short times, in agreement with our assumption that interactions between elements are negligible during the early primary creep regime, as shown by the study of spatial damage structure (section 4.3). This result justifies our assumption that $\epsilon(t)$ is constant, equal to the initial elastic strain σ/E_0, in order to derive the approximate relations for the damage rate (29,30).

5.4. Tertiary creep regime

After the primary creep regime, the strain rate and the damage rate increase due to interactions between elements and due to increasing damage. The time-to-failure of each element decreases on average with time because:

- the stress on undamaged elements increases on average after an avalanche, therefore the failure time estimated from (4) or (3) decreases;
- the time-to-failure of undamaged elements also decreases with time because the fraction of consumed failure time $p_i(n)$ in (9) increases with time;
- for damaged elements, the time-to-failure decreases proportionally to the damage $t_i(n) - t(n) \sim (1 - D_0)^n$, if equation (12) is used to update the time-to-failure of damaged elements.

We can explain the power-law singularity of the damage rate (17) in the tertiary creep regime in the case where the time-to-failure decreases with the damage (12). In this case, the main mechanism leading to the power-law acceleration of the damage rate is the decrease of the time-to-failure between 2 damage events. In this case, we can simplify the model by

• neglecting interactions between events, assuming that the stress on all elements does not change with time and is equal to the externally applied stress $\sigma_i = \sigma$. Therefore the time-to-failure of element i changes only when it is damaged, i.e., when $t = t_i(n)$, where n is the number of damage events of element i. And only one element breaks during each avalanche ($s = 1$).

• neglecting heterogeneity of strength, i.e., assuming $\sigma_{0,i}$ is equal to the average strength σ_0 for all elements, in order to compute the average failure time of an element. In the numerical simulations, the elements that break have on average a strength smaller that the average strength σ_0 (shorter time-to-failure). Thus assuming $\sigma_{0,i} = \sigma_0$ overestimates the time t_c of the global failure. But this should not affect the temporal behavior of the damage rate derived below. Because in the tertiary creep regime all elements have been damaged several times, and because the strength is redrawn randomly after each damage event, assuming that $\sigma_{0,i}$ is constant is not too unrealistic, and allows us to derive simple analytical solutions.

Under these assumptions, and using (12) recursively for all damage events, the time-to-failure $t_i(n)$ of element i after the n^{th} damage event is given by

$$\begin{aligned} t_i(n) &= t_i(n-1) + t_f(\sigma,\sigma_0)\,(1-D_0)^n \\ &= t_i(0) + t_f(\sigma,\sigma_0)\sum_{j=1}^{n}(1-D_0)^j \\ &= t_i(0) + t_f(\sigma,\sigma_0)\,(1-D_0)\sum_{j=0}^{n-1}(1-D_0)^j \\ &= t_i(0) + t_f(\sigma,\sigma_0)\;(1-D_0)\,\frac{1-(1-D_0)^n}{D_0} \\ &= t_f(\sigma,\sigma_0)\,\frac{1-(1-D_0)^{n+1}}{D_0} \end{aligned} \tag{36}$$

The time between 2 damage events of element i is given by, using (36),

$$\begin{aligned} \Delta t &= t_i(n+1) - t_i(n) \\ &= t_f(\sigma,\sigma_0)\,(1-D_0)^{n+1} \\ &= t_f(\sigma,\sigma_0) - D_0\,t_i(n) \end{aligned} \tag{37}$$

The rate of damage at time $t = t_i(n)$ for the system of N independent elements is given by

$$\dot{n}(t) = \frac{N}{\Delta t} = \frac{N}{t_f(\sigma,\sigma_0) - D_0 t} = \frac{N}{D_0(t_c - t)}\,, \tag{38}$$

where t_c is the time of the macroscopic failure of the system, corresponding to the singularity of damage and deformation, which is given by

$$t_c = \frac{t_f(\sigma,\sigma_0)}{D_0}\,. \tag{39}$$

Expression (38) describes a power-law singularity of the damage rate, similar to the numerical simulations (17) with $p'_n = 1$.

In this simplified model, the strain at time $t = t_i(n)$ obeys

$$\begin{aligned} \epsilon(t) &= \frac{\sigma}{E} = \frac{\sigma}{E_0(1-D_0)^n} \\ &= \frac{\sigma}{E_0}\,\frac{1-D_0}{1-D_0\,t/t_f(\sigma,\sigma_0)} \\ &= \frac{\sigma}{E_0 D_0}\,\frac{t_f(\sigma,\sigma_0)}{(t_c - t)} \end{aligned} \tag{40}$$

and the strain rate is

$$\dot{\epsilon}(t) = \frac{\sigma}{E_0 D_0}\,\frac{t_f(\sigma,\sigma_0)}{(t_c - t)^2} \tag{41}$$

corresponding to a value $p'_\epsilon = 2$ in (16). This analysis explains qualitatively the power-law singularity of the strain rate and of the rate of damage events found in the simulation, and the fact that $p'_\epsilon > p'_n$ (strain rate accelerates faster than damage rate).

These results suggest that interactions between elements are not essential to obtain a power-law acceleration of damage and strain during tertiary creep. Indeed, our simple analytical model described above, which neglects interactions, produces a power-law acceleration (41). But the values $p'_n = 1$ and $p'_\epsilon = 2$ in our analytical study are larger than the values $p'_n \approx 0.8$ and $p'_\epsilon \approx 1.3$ observed in the numerical simulations. Expressions (40), (41), and (38) are consistent (in the limit where $N \gg D_0$) with the relation between the damage rate, strain and strain rate given in (24).

If the time-to-failure of each element does not depend on damage, i.e., if (11) is used to update the time-to-failure of broken elements, then the recurrence time is constant $\Delta t = t_f(\sigma,\sigma_0)$. The damage rate is also constant $\dot{n}(t) = N/t_f(\sigma,\sigma_0)$. In contrast, in the numerical simulations we found that the damage rate increases linearly with time in this case. For the strain rate, relation (24) predicts an exponential increase of the strain and strain rate (assuming $N \gg D_0$), as observed in the numerical simulations

$$\epsilon(t) = \frac{\sigma}{E_0}\,\exp\left(\frac{D_0\,t}{t_f(\sigma,\sigma_0)}\right) \tag{42}$$

$$\dot{\epsilon}(t) = \frac{\sigma}{E_0}\,\frac{D_0}{t_f(\sigma,\sigma_0)}\,\exp\left(\frac{D_0\,t}{t_f(\sigma,\sigma_0)}\right)\,. \tag{43}$$

In both cases, we found that the analytical expressions for the damage rate and for the strain rate predict an increase during tertiary creep that is slower than in the numerical simulations. The main factor that can explain these differences are elastic interactions between elements. Elastic interactions produce a spatial correlation of the stress, damage, and strength fields. As a consequence, the mean size of damage events increases with time, because avalanches can more easily propagate at larger distances. In contrast, our simple analytical study assumes a constant avalanche size. The power-law increase of the average event size with time may thus explain why the strain and damage acceleration during tertiary creep is faster (larger exponents p') in our simulations than in this simple analytical study.

6. Discussion

We have first analyzed experimental data to characterize the relation between the applied stress and the time-to-failure. We found that the exponential (3) and the power-law (4) relations cannot be distinguished from observations of creep experiments; both laws fit the data equally well. In both cases, the exponent b and b' are very large, showing that a small stress change produces a huge variation of the time-to-failure. Other factors, such as temperature or water saturation, also strongly influence the time-to-failure. These factors should be taken into account when modeling geological objects. The impact of the b-exponent in the numerical simulations is weak and only changes the time scale, i.e., the time of macroscopic failure.

In order to model the time-dependent damage of rocks, we use these experimental laws at the scale of each element to estimate its time-to-failure as a function of its stress history. A broken element is damaged by decreasing its Young's

modulus. The scale of each element is supposed to be much larger than the crack size. Elastic interactions between elements and heterogeneity of the mechanical properties lead to the emergence of a complex macroscopic behavior, which is different from the behavior of individual elements. The major interest of this model is to simulate at the same time the temporal evolution of damage and strain, the distribution of acoustic emission events, and the progressive damage localization.

In our model, we find that the time of macroscopic failure is proportional to the time-to-failure used as input at the scale of each element. The transition time between primary and tertiary creep is also proportional to the time of macroscopic failure. This suggests that the evolution of strain rate or acoustic emission during primary and secondary creep can be used to forecast the time of macroscopic failure of an object. A similar conclusion was reached by *Scholz* [1972], based on creep experiments, who suggested that "microfracturing appears to be completely diagnostic of static fatigue, since the rate of microfracturing and the average time-to-failure behave similarly", i.e., the only characteristic time for the evolution of the damage rate during creep is the time of macroscopic failure. This is in agreement with the experimental and analytical results of *Nechad et al.* [2005a] for heterogeneous material: the macroscopic failure time was proportional to the duration of the primary creep regime.

During primary creep, we observe a power-law decrease of the rate of strain, damage event and released energy during primary creep, with an exponent ≈ 0.8. This value is comparable to the one observed for metal's [*Andrade*, 1910], for glass/polyester composite materials [*Nechad et al.*, 2005a], and for earthquake aftershocks [*Omori*, 1894]. In our model, the power-law decay of damage, strain and energy rate at short times can be explained by the increase of the time-to-failure with the strength coupled with the heterogeneity of the initial strength of each element. A few other models have also reproduced this law for the relaxation of strain rate during primary creep [*Lockner*, 1993b, 1998; *Nechad et al.*, 2005a]. In our simulations, the exponents p_n, p_W and p_ϵ are weakly sensitive to the applied stress and to the time-to-failure law used as input. During this regime, the damage is spatially non-correlated in our simulations (the correlation length is zero).

The secondary creep regime does not appear clearly in the numerical simulations, and can be rather defined as the transition between primary and tertiary creep, corresponding to the minimum value of the strain rate. Note that for very low stress values, one should take into account the self-healing and blunting of cracks, which may prevent subcritical crack growth. Therefore, there may be a minimum value of the applied stress under which a rock never fail, but continue to deform at a constant rate, or eventually stops to deform. In contrast, our model predicts that the system will always fail (reach the critical strain ϵ_c) in finite time, even for a very small applied stress.

The tertiary creep regime is characterized by an increase of the strain rate, the energy rate, and the damage rate ending by macroscopic failure. This acceleration follows a power-law as a function of the remaining time before failure if the time-to-failure of each element increases with damage according to (12). Otherwise, the acceleration of the strain and damage is slower, roughly linear with time for the rate of damage events, and exponential for the strain rate. The power-law acceleration of damage in our model is similar to the experiments of *Guarino et al.* [e.g. 2002] and *Nechad et al.* [2005a]. At a larger scale, the same behavior was observed for the increase in micro-seismicity recorded before a cliff collapse [*Amitrano et al.*, 2005]. They observed a power law acceleration of both the event number and the seismic energy release until the collapse of the chalk cliff.

Damage localization emerges during tertiary creep, with the appearance of a non-zero correlation length (Figures 8 and 9). The spatial correlation length further increases during tertiary creep, in agreement with the critical point theory, which predicts a power-law divergence of the correlation length [*Stanley*, 1971]. The tertiary creep ends with the macroscopic failure of the model, i.e., the complete damage localization. These results are in agreement with laboratory creep experiment showing that damage becomes localized before failure [*Hirata et al.*, 1987]. The damage localization is often characterized by a decrease of the fractal dimension of the cloud of damage events [e.g. *Lockner*, 1993a; *Hirata et al.*, 1987]. The limited size of our numerical model does not allow us to calculate the fractal dimension.

The final structure of the damage systematically shows a shear band (Figure 7). The thickness of the bands and their orientation relative to the applied stress decrease with the applied stress. To our knowledge, this relationship between the thickness of the shear band and the applied stress has not yet been observed in creep experiments. This could be explained by the scarcity of creep tests with very low applied stress, i.e., $\sigma/\sigma_0 < 0.5$, because of technical difficulties for measuring low strain rates over times as long as several years [*Berest et al.*, 2005]. Previous experimental studies have observed a damage localization along shear bands similar to our model [*Jaeger and Cook*, 1979; *Kranz*, 1983; *Ramsey and Chester*, 2004]. These studies observed a transition between a brittle (localized damage) to a ductile (diffuse deformation) behavior as the confining pressure increases. *Amitrano et al.* [1999] reproduced this localized/diffuse transition with the time-independent version of our model. In this model, the thickness of the band increases and its orientation relatively to the major stress decreases as the confining pressure increases. This transition between a localized and diffuse behavior can be explained by the decrease of the slope of the failure criterion (friction coefficient) as the confining pressure increases. The change of the friction coefficient modifies the geometry of the damage zone after each damage event, and thus the damage localization [*Amitrano et al.*, 1999; *Amitrano*, 2003]). This change of behavior with the confining pressure cannot explain the localized/diffuse transition in our model because the failure criterion is kept constant and no confining pressure is applied. Further investigations are needed to understand this new kind of diffuse/localized transition as a function of the applied stress.

This numerical result could be helpful for interpreting geological structures such as faults. The thickness of the damaged area surrounding a fault has been proposed to increase with its tangential displacement [e.g. *Vermilye and Scholz*, 1998], but this result is very controversial [see *Evans*, 1990]. *Evans* [1990] wrote that "thickness-displacement relationship may exist for some populations, but may vary between populations depending on fault type, rock rheology and environmental parameters". Our model indicates that the thickness of the damage zone surrounding a fault should be larger in zones of low σ/σ_0 values (or low strain rate) and lower in zones with high σ/σ_0 values (or high strain rate). These results should be validated by field observations in areas where the tectonic stress/strain regime is known, and could explain the variability of damage zone thickness.

In our model, the event size distribution appears to depends on time and on stress. For low stress values, the mean size increases with time and the power-law distribution appears only when integrating over the whole simulation. For larger stress, the power-law distribution is observed from the beginning of the simulation and does not change as the macroscopic failure approaches. The results for large stress are similar to the creep experiments of *Nechad et al.* [2005b], who did not observe any change of $P(\Delta W, t)$ with time. *Amitrano et al.* [2005] observed an increase with time of the average energy of seismic events preceding a cliff collapse, which was interpreted either as a decrease of β with time,

or as a constant β-exponent for small energies, with an exponential falloff above some typical energy ΔW_c increasing with time. A similar behavior has been observed during a creep test on porous rocks with increasing stress steps [*Amitrano*, 2005]. The size distribution of acoustic emissions shows a transition between an exponential fall-off for low stress to a pure power-law with decreasing β for larger stress. In contrast, *Guarino et al.* [2002] observed an increase of the β exponent as the stress increases during creep test on artificial heterogeneous materials.

7. Conclusion

We propose a numerical model based on static fatigue laws in order to model the time-dependent damage and deformation of rocks. A time-to-failure law, established experimentally at the scale of a sample, is used to simulate the behavior of each element of our finite element model. Elastic interactions coupled with material heterogeneity lead to the emergence of a macroscopic behavior that is richer than the elementary one. In particular, we observe primary and tertiary creep regimes associated respectively with a power-law decay and increase of the rate of strain, damage event and energy release. Our model also produces a power-law distribution of damage event sizes, and damage localization along shear bands. This model thus reproduces many properties of rock creep, which were previously not modeled simultaneously.

Our approach thus appears to be an interesting and promising alternative to the microscopic approach, dedicated to the study of fracture propagation, and to the macroscopic approach based on constitutive laws. It shows that the complex behavior of creeping rocks observed at a given scale may result from the interactions of elements at a smaller scale.

In this paper, we have considered only the case of a stress step (creep), but we could simulate any arbitrary time-dependent loading, imposing either the applied stress, strain, or strain rate. Note that our model has an elastic-brittle behavior. Therefore the strain is entirely reversible; removing the applied stress brings the strain back to zero. In contrast, real rocks have some viscous irreversible deformation. We could modify the behavior of each element in our model to take into account this effect, e.g., by integrating permanent deformation steps associated with damage.

Acknowledgments. We thank J.-R. Grasso and M. Freyssines for useful discussions. We are grateful to the associate editor W. P. Schellart, and to the two anonymous reviewers for careful reviews and useful suggestions.

References

Amitrano, D. (2003), Brittle-ductile transition and associated seismicity: Experimental and numerical studies and relationship with the b-value, *J. Geophys. Res.*, *108*(B1), 2044, doi:10.1029/2001JB000,680.

Amitrano, D. (2004), Emerging complexity in a simple model of the mechanical behavior of rocks, *CR Geosciences*, *336*(6), 505–512 (doi:10.1016/j.crte.2003.11.023).

Amitrano, D. (2005), Complexite et dynamique de l'endommagement et de la rupture, mecanique, sismicite et invariance d'echelle des objets geologiques, Habilitation a diriger les recherches, INPL.

Amitrano, D. (2006), Failure by damage accumulation in rocks, *International Journal of Fracture*, p. In press.

Amitrano, D., J.-R. Grasso, and D. Hantz (1999), From diffuse to localized damage through elastic interaction, *Geophysical Research Letters*, *26*(14), 2109–2112.

Amitrano, D., J. Grasso, and G. Senfaute (2005), Seismic precursory patterns before a cliff collapse and critical-point phenomena, *Geophys. Res. Let.*, *32*(8), L08,314, doi:10.1029/2004GL022,270.

Andrade, E. N. (1910), The viscous flow in metals, and allied phenomena, *Proc. R. Soc. A*, *84*, 1–12.

Atkinson, B. (1991), *Fracture mechanics of rock*, Geology series, Academic press.

Atkinson, B. K. (1984), Subcritical crack growth in geological materials, *J. Geophys. Res.*, *89*, 4077–4114.

Baud, P., and P. Meredith (1997), Damage accumulation during triaxial creep of darley dale sandstone from pore volumetry and acoustic emission, *Int. J. Rock Mech. Min. Sci. and Geomech. Abstr.*, *34*(3-4), Paper No 24, pp 1–8.

Berest, P., P. Blum, J. Charpentier, H. Gharbi, and F. Vales (2005), Very slow creep tests on rock samples, *Int. J. Rock Mech. Min. Sci.*, *42*, 569–576.

Boukharov, G., M. Chanda, and N. Boukharov (1995), The three processes of brittle crystalline rock creep, *Int. J. Rock Mech. Min. Sci. and Geomech. Abstr.*, *32*(4), 325–335.

Caine, N. (1980), The rainfall intensity-duration control debris-flows, *Geografiska Annaler*, *62 A*, 23–27.

Charles, R. (1958), The static fatigue of glass, *J. Appl. Phys.*, *29*, 1549–1560.

Ciliberto, S., A. Guarino, and R. Scoretti (2001), The effect of disorder on the fracture nucleation process, *Physica D*, *158*(1-4), 83–104.

Coleman, B. D. (1956), Time dependence of mechanical breakdown phenomena, *J. Appl. Phys.*, *27*, 862–866.

Coleman, B. D. (1958), Statistics and time dependence of mechanical breakdown in fibers, *J. Appl. Phys.*, *29*, 968–983.

Cook, R. F. (1986), Crack propagation thresholds: A measure of surface energy, *J. Mat. Res.*, *1*, 852–860.

Cruden, D. (1974), The static fatigue of brittle rock under uniaxial compression, *Int. J. Rock Mech. Min. Sci. and Geomech. Abstr.*, *11*, 67–73.

Das, S., and C. Scholz (1981), Theory of time-dependent rupture in the earth, *J. Geophys. Res.*, *86*(B7), 6039–6051.

Di Giovambattista, R., and Y. Tyupkin (2001), An analysis of the process of accelaration of seismic energy in laboratory experiments on destruction of rocks and before earthquakes on kamchatka and in italy, *Tectonophysics*, *338*, 339–351.

Evans, J. (1990), Thickness-displacement relationships for fault zones, *Journal of Structural Geology*, *12*(8), 1061–1065.

Freiman, S. W. (1984), Effects of chemical environments on slow crack growth in glasses and ceramics, *J. Geophys. Res.*, *89*, 4072–4076.

Guarino, A., S. Ciliberto, and A. Garcimartin (1999), Failure time and microcrack nucleation, *Europhysics letters*, *47*(4), 456–461.

Guarino, A., S. Ciliberto, A. Garcimartin, M. Zei, and R. Scoretti (2002), Failure time and critical behavior of fracture precursors in heterogeneous materials, *Eur. Phys. J. B*, *26*(doi: 10.1140/epjb/e20020075), 141–151.

Helmstetter, A., D. Sornette, and J.-R. Grasso (2003), Mainshocks are aftershocks of conditional foreshocks: How do foreshock statistical properties emerge from aftershock laws, *J. Geophys. Res.*, *108*(B1), 2046, doi:10.1029/2002JB001,991.

Hidalgo, R., F. Kun, and H. Herrmann (2002), Creep rupture of viscoelastic fiber bundles, *Phys. Rev. E*, *65*, 032,502.

Hirata, T., T. Satoh, and K. Ito (1987), Fractal structure of spacial distribution of microfracturing in rock, *Geophys. J. R. astr. Soc.*, *90*, 369–374.

Jaeger, J. C., and N. G. W. Cook (1979), *Fundamentals of rock mechanics*, Chapman and Hall, London.

Kagan, Y. (1999), Universality of the seismic moment-frequency relation, *Pageoph*, *155*, 537–573.

Katz, O., and Z. Reches (2004), Microfracturing, damage, and failure of brittle granites, *J. Geophys. Res.*, *109*(B1), B01,206, 10.1029/2002JB001,961.

Kawada, Y., and H. Nagahama (2004), Viscoelastic behavior and temporal fractal properties of lherzolite and marble: possible extrapolation from experimental results to the geological time-scale, *Terra Nova*, *16*, 128–132, doi: 10.1111/j.1365–3121.2004.00,540.x.

Kemeny, J., and N. G. W. Cook (1986), Effective moduli, nonlinear deformation and strength of a cracked elastic solid, *Int. J. Rock Mech. Min. Sci. and Geomech. Abstr.*, *23*(2), 107–118.

Kranz, R. (1980), The effect of confining pressure and difference stress on static fatigue of granite, *J. Geophys. Res.*, *85*(B4), 1854–1866.

Kranz, R. (1983), Microcracks in rocks: a review, *Tectonophysics*, *100*, 449–480.

Kranz, R., W. Harris, and N. Carter (1982), Static fatigue of granite at 200c, *Geophys. Res. Let.*, *9*(1), 1–4.

Lockner, D. (1993a), The role of acoustic emission in the study of rock fracture, *Int. J. Rock Mech. Min. Sci. and Geomech. Abstr.*, *30*(7), 883–899.

Lockner, D. (1993b), Room temperature creep in saturated granite, *J. Geophys. Res.*, *98*, 475–487.

Lockner, D. (1998), A generalized law for brittle deformation of westerly granite, *J. Geophys. Res.*, *103*(B3), 5107–5123.

Lockner, D., and J. Byerlee (1980), Development of fracture planesduring creep in granite, in *Second Conference on Acoustic Emission/Microseismic Activity in Geological Structures and Materials*, pp. 11–25, Trans Tech Publication, Clausthal-Zellerfeld, Germany.

Lockner, D., and T. Madden (1991a), A multiple-crack model of brittle fracture 1. non-time dependant simultations, *Journal of Geophysical Research*, *96*(B12), 19,623–19,642.

Lockner, D., and T. Madden (1991b), A multiple-crack model of brittle fracture 2. time dependant simultations, *Journal of Geophysical Research*, *96*(B12), 19,643–19,654.

Lockner, D., J. Byerlee, V. Kuskenko, A. Ponomarev, and A. Sidorin (1991), Quasi-static fault growth and shear fracture energy in granite, *Nature*, *350*, 39–42.

Main, I. (2000), A damage mechanics model for power-law creep and earthquake aftershock and foreshock sequences, *Geophys. J. Int.*, *142*, 151–161.

Masuda, K. (2001), Effects of water on rock strength in a brittle regime, *Journal of Structural Geology*, *23*, 1653–1657.

Miguel, M.-C., A. Vespignani, M. Zaiser, and S. Zapperi (2002), Dislocation jamming and andrade creep, *Phys. Rev. Lett*, *89*(16), 165,501.

Miura, K., Y. Okui, and H. Horii (2003), Micromechanics-based prediction of creep failure of hard rock for long-term safety of high-level radiactive waste disposal system, *Mechanics of Materials*, *35*, 587–601.

Moore, D., and D. Lockner (1995), The role of microfracturing in shear-fracture propagation in granite, *Journal of Structural Geology*, *17*, 95–114.

Nechad, H., A. Helmstetter, R. E. Guerjouma, and D. Sornette (2005a), Andrade creep and critical time-to-failure laws in heterogeneous materials, *Phys. Rev. Lett*, *94*, 045,501.

Nechad, H., A. Helmstetter, R. E. Guerjouma, and D. Sornette (2005b), Andrade and critical time-to-failure laws in fiber-matrix composites: Experiments and model, *Journal of Mechanics and Physics of Solids*, *53*(5), 1099–1127.

Ngwenya, B. T., I. G. Main, and S. C. Elphick (2001), A constitutive law for low-temperature creep of water-saturated sandstones, *J. Geophys. Res.*, *106*, 21,811–21,826.

Omori, F. (1894), On the aftershocks of eathquakes, *J. Coll. Sci. Imp. Univ. Tokyo*, *7*(111-120).

Perfettini, H., and J.-P. Avouac (2004), Postseismic relaxation driven by brittle creep: A possible mechanism to reconcile geodetic measurements and the decay rate of aftershocks, application to the chi-chi earthquake, taiwan, *J. Geophys. Res.*, *109*(B2), B02,304, doi: 10.1029/2003JB002,488.

Petley, D., M. Bulmer, and W. Murphy (2002), Patterns of movement in rotational and translational landslides, *Geology*, *30*(8), doi: 10.1130/0091–7613, 719–722.

Politi, A., S. Ciliberto, and R. Scorretti (1995), Failure time in the fibre-bundle model with thermal noise and disorder, *Physical Review E*, *66*(2), 026,107/1–6.

Pradhan, S., and B. K. Chakrabarti (2003), Failure properties of fiber bundles, *Int. J. Mod. Phys. B*, *17*, 5565–5581.

Purnell, P., N. Short, and C. Page (2001), A static fatigue model for the durability of glass reinforced cement, *Journal of Materials Science*, *36*, 5385–5390.

Ramsey, J., and F. Chester (2004), Hybrid fracture and the transition from extension fracture to shear fracture, *Nature*, *428*, 63 – 66, doi:10.1038/nature02,333.

Ray, S., M. Sarkar, and T. Singh (1999), Effect of loading an strain rate on the mechanical behaviour of sandstone, *Int. J. Rock Mech. Min. Sci.*, *36*, 543–549.

Reches, Z., and D. Lockner (1994), Nucleation and growth of faults in brittle rocks, *Journal of Geophysical Research*, *99*(B9), 18,159–18,173.

Saito, M. (1965), Forecasting the time of occurrence of a slope failure, in *Proc. 6th Int. Conf. Soil Mech. and Found. Eng.*, vol. 2, pp. 537–541, Montral.

Saito, M. (1969), Forecasting time of slope failure by tertiary creep, in *Proc. 7th Int. Conf. Soil Mech. and Found. Eng.*, vol. 2, pp. 677–683, Mexico City.

Saito, M., and H. Uezawa (1961), Failure of soil due to creep, in *Proc. 5th Int. Conf. Soil Mech. and Found. Eng.*, vol. 1, pp. 315–318, Montral.

Scholz (1968a), Microfracturing and the inelastic deformation of rocks in compression, *J. Geophys. Res.*, *73*, 1417–1432.

Scholz, C. (1968b), Mechanism of creep in brittle rock, *J. Geophys. Res.*, *73*(10), 3295–3302.

Scholz, C. (1972), Static fatigue of quartz, *J. Geophys. Res.*, *77*(11), 2104–2114.

Shaw, B. (1993), Generalized omori law for aftershocks and foreshocks from a simple dynamics, *Geophys. Res. Let.*, *20*, 907–910.

Shcherbakov, R., and D. Turcotte (2003), Damage and self-similarity in fracture, *Theoretical and Applied Fracture Mechanics*, *39*(3), 245–258.

Sornette, D., and C. Vanneste (1994), Dendrites and fronts in a model of dynamical rupture with damage, *Phys. Rev. E*, *50*, 4327–4345.

Stanley, H. (1971), *Introduction to phase transition and critical phenomena*, Oxford University Press.

Sue, C., J. Grasso, F. Lahaie, and D. Amitrano (2002), Mechanical behavior of western alpine structures inferred from statistical analysis of seismicity, *Geophysical Research Letters*, *29*(8, doi:10.1029/2001GL014050), 65–1 65–4.

Turcotte, D., W. Newman, and R. Shcherbakov (2003), Micro and macroscopic models of rock fracture, *Geophys. J. Int.*, *152*(3), 718–728.

Vermilye, J., and C. Scholz (1998), The process zone: A microstrucutral view of fault growth, *J. Geophys. Res.*, *103*(B6), 12,223–12,237.

Voight, B. (1988a), A method for prediction fo volcanic eruption, *Nature*, *332*, 125–130.

Voight, B. (1988b), Materials science laws applies to time forecast of slope failure, in *5th Int. Symp. Landslides Lausanne 1988*, vol. 3, edited by Bonnard, pp. 1471–1472, Balkema, Lausanne.

Voight, B. (1989), A relation to describe rate-dependent material failure, *Science*, *243*, 200–203.

Vujosevic, M., and D. Krajcinovic (1997), Creep rupture of polymers – a statistical model, *Int. J Solid Structures*, *34*(9), 1105–1122.

Wiederhorn, S. M., and L. H. Bolz (1970), Stress corrosion and static fatigue of glass, *J. Am. Ceram. Soc.*, *50*, 543.

David Amitrano, LIRIGM-LGIT, Grenoble University, Maison des Geosciences, 1381 rue de la Piscine, BP 53, 38041 Grenoble Cedex 9, 38042 France (email: david.amitrano@ujf-grenoble.fr)

Agnès Helmstetter, LGIT, Grenoble University, Maison des Geosciences, 1381 rue de la Piscine, BP 53, 38041 Grenoble Cedex 9, 38042 France (email: agnes.helmstetter@ujf-grenoble.fr)

Table 1. Mathematical symbols

Symbol	Eq. or section	Description
α	(19)	Orientation relative to major stress
a, B	(32, 1)	Constants
$A(\alpha)$	(20)	Characteristics of damage
b, b'	(3,4)	Exponent of time-to-failure laws
β	4.2	Exponent of the energy pdf
C, C_1, C_2	(7)	Cohesion, min and max initial values
C_{H20}	(2)	Water concentration
$D_0 = 0.1$	(5)	Constant damage parameter
$D_i(n)$, D	(6)	Damage of element i after n events
DSC	(19)	Damage correlogram
$E_0 = 50$ GPa,	(5)	Young modulus (initial, average,
$< E >$, $E_{i,n}$	(5)	and for element i after n events)
ϵ, $\epsilon_c = 0.03$	3	Strain, final strain
$\phi = 60^o$	(7)	Internal friction angle
K, K_c	(1,2)	Intensity factor, critical value
L	(2)	Crack length
λ, λ_c	(19)	Distance, correlation length
$N = 640$	(21)	Number of elements in the model
n	(5)	Number of damage events
$\nu = 0.25$	(3)	Poisson coefficient
$P(W,t)$	4.2	Energy pdf at time t
p_n, p_ϵ, p_W	(13-15)	Exponents of damage, energy and strain rate for primary creep
p'_N, p'_ϵ, p'_W	(16-18)	Exponents for tertiary creep
$p_i(n)$	(9)	Fraction of consumed time-to-failure
q	(2)	Exponent of subcritical crack growth
r	(19)	Linear correlation coefficient
R	(1)	Gas constant
s	(21)	Avalanche size
σ	(3)	Mean major stress
σ_i	(11)	Major stress on element i
σ_0, $\sigma_{0,i}$	(1,7)	Strength, average and for element i
σ_{0_1}, σ_{0_2}	(29)	Min and max initial strength
$\sigma_1, \sigma_2, \sigma_3$	(7)	Major, intermediate and minor main stress
T	(1)	Temperature
$t(n)$	(11)	Time of n^{th} damage event
$t_i(n)$	(11)	Failure time of element i after n events
$t_f(\sigma, \sigma_0)$	(3,4)	Time-to-failure
t_c	(16)	Time of macroscopic failure
t_m		Transition time, primary to tertiary creep
Δt	(23)	Average inter-event time
$t_0 = 1$, $t'_0 = 1$	(3,4)	Characteristic time
V, V_0	(1)	Crack growth velocity
W	(15)	Cumulated elastic energy release
W_0	(1)	Activation energy
W_c		Typical energy (fall off for large W)
ΔW	(25)	Change of elastic energy after a damage event

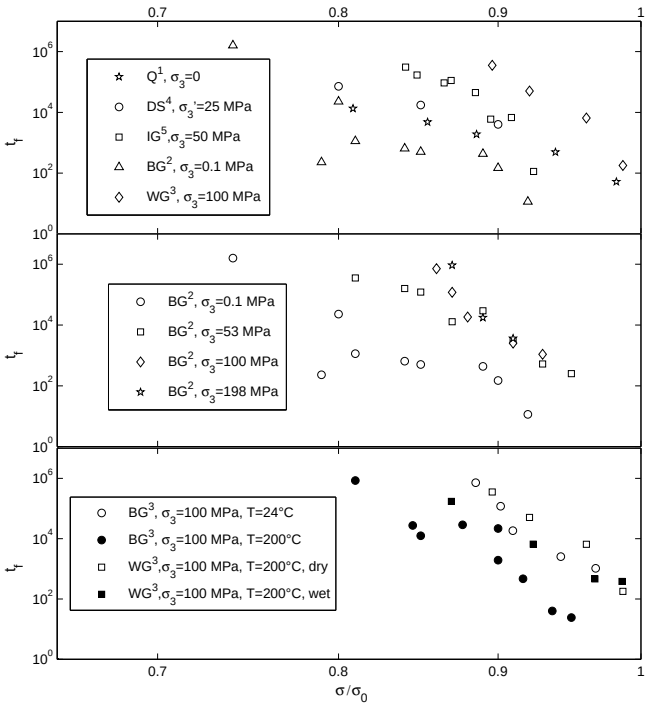

Figure 1. Failure time (in sec) for laboratory creep tests with a variety of loading conditions, realized by different studies (1) [*Scholz*, 1972], (2) [*Kranz*, 1980], (3) [*Kranz et al.*, 1982], (4) [*Baud and Meredith*, 1997], (5) [*Masuda*, 2001]. The tests presented in the upper plot concern different rock types: BG: Barre granite, WG: Westerly granite, IG: Indiana granite, DS: Darley Dale sandstone. The applied stress σ is normalized by the instantaneous strength σ_0 (estimated by the strength for short failure times). For [*Baud and Meredith*, 1997], the tests were performed at constant pore pressure $P_p = 50$ MPa and confining pressure $\sigma_3 = 75$ MPa. In this case, the legend indicates the effective confining pressure $\sigma'_3 = \sigma_3 - P_p = 25$ MPa. The middle plot shows the impact of the confining pressure on the time-to-failure of Barre Granite. The lower plot shows the impact of temperature and water saturation. respectively.

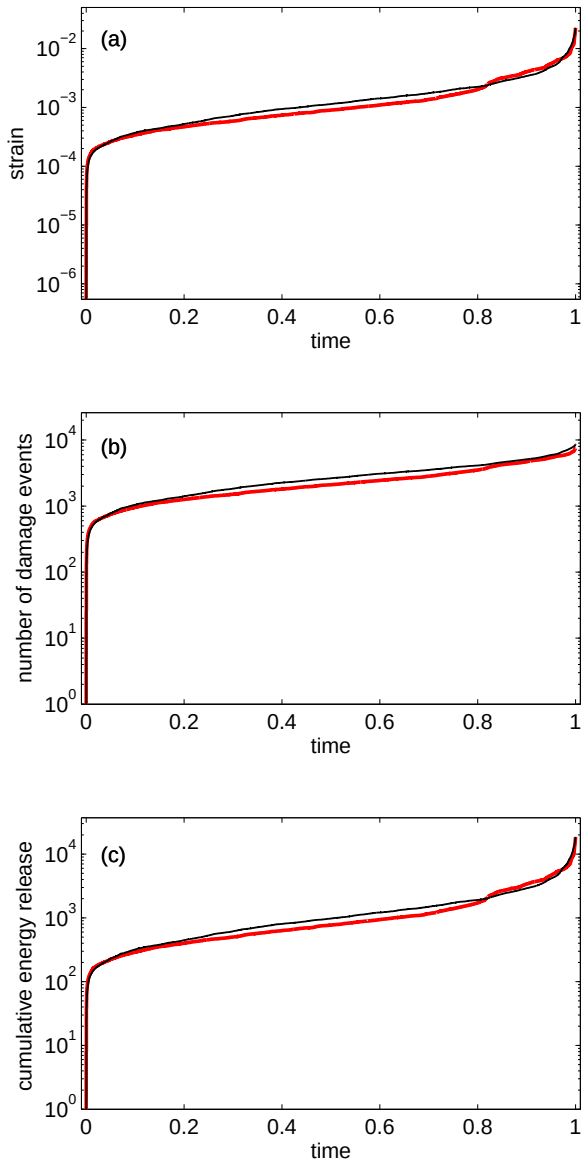

Figure 2. Typical temporal evolution of (a) strain (removing the initial elastic strain), (b) number of damage events, and (c) energy release, for two simulations with $\sigma/\sigma_0 = 0.80$, and using a power-law relation (4) with b'=40 (thick gray line), or an exponential (3) (thin black line) time-to-failure relation with b=40. Time is normalized by the macroscopic failure time.

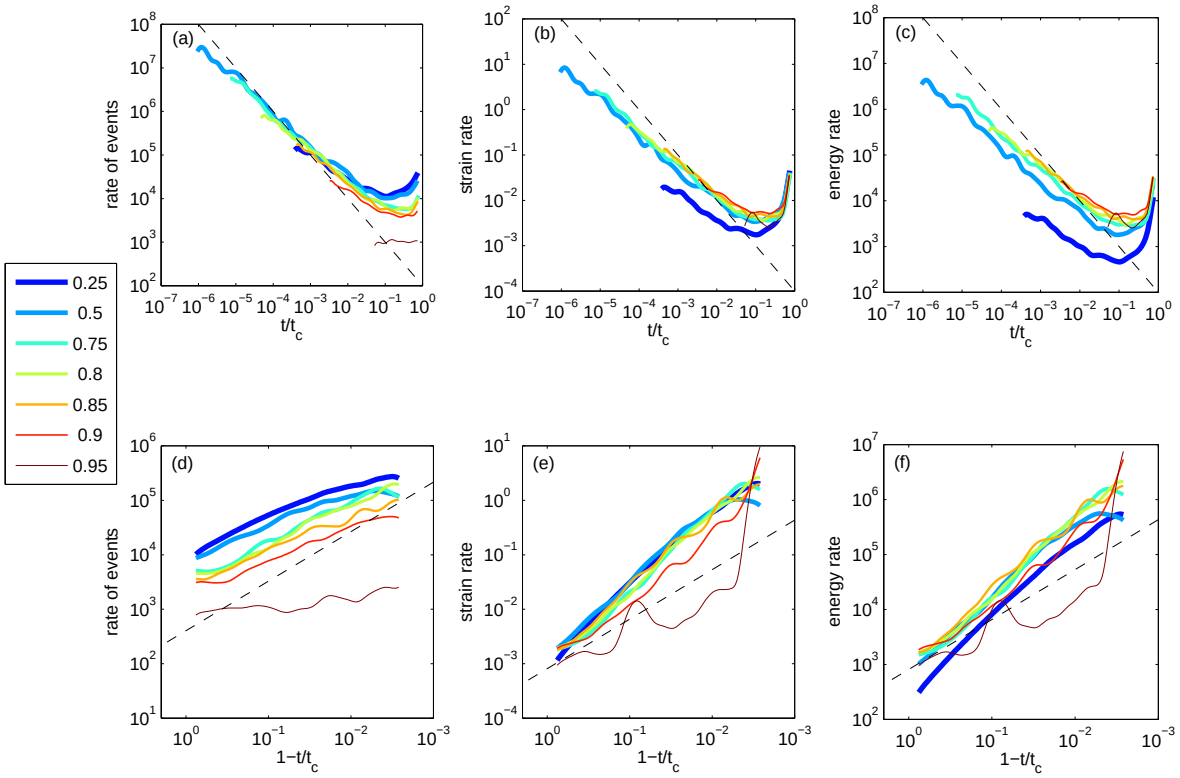

Figure 3. Rate of damage events (a,d), strain (b,e), and energy (c,f) for different values of the applied stress σ/σ_0 (see caption), using the exponential time-to-failure law (3) with b=40, and using expression (12) for the time-to-failure of each element as a function of damage, stress and strength. The upper and lower plots show the same data with different axes, to illustrate the power-law decay during primary creep and the power-law acceleration during tertiary creep. In each plot the dashed black line represents a power-law relation with exponent of 1 for reference.

Table 2. Results of the fits for both the exponential (3) and the power law (4) time-to-failure relations, using data from the literature. We have estimated the parameters $\log(t_0)$ or $\log(t'_0)$ and b or b' using a linear regression in semilog or loglog plots for the exponential and power-law relations respectively. r is the correlation coefficient, and N_p the number of creep tests.

Ref.[a]	Rock Type	T °C	dry/ wet	σ_3 MPa	σ_0 MPa	N_p	Exponential fit (3) b	$\log(t_0)$	r	Power-law fit (4) b'	$\log(t'_0)$	r
S72[b]	quartz, *c*-axis	25	wet	0	2070	62	28.	32.	0.82	24.	4.4	0.82
S72[c]	quartz, *a*-axis	25	wet	0	1950		73.	82.		73.	5.7	
K80	Barre granite	room	dry	0.1		9	48.	47.	0.83	40.	0.2	0.84
K80	Barre granite	room	dry	53		8	55.	58.	0.97	48.	3.4	0.97
K80	Barre granite	room	dry	100		5	88.	88.	0.96	79.	0.7	0.96
K80	Barre granite	room	dry	198		3	138.	134.	0.97	123.	3.8	0.97
K82	Barre granite	24	dry	100		5	78.	82.	0.96	73.	3.9	0.97
K82	Barre granite	200	dry	100		9	69.	69.	0.93	60.	0.9	0.92
K82	Westerly granite	200	dry	100		4	79.	83.	0.98	74.	4.9	0.98
K82	Westerly granite	200	wet	100		4	55.	60.	0.99	51.	4.8	0.99
M91	Indiana granite	room	dry	0		8	82.	83.	0.93	72.	0.8	0.92
BM97	Darley Dale sandstone	room	dry	30		3	29.	34.	$> .99$	24.	5.7	$> .99$

[a] References: BM97: *Baud and Meredith* [1997]; M91 : *Masuda* [2001]; K80: *Kranz* [1980]; K82: *Kranz et al.* [1982]; S72: *Scholz* [1972].

[b] Data from Figure 1 of [*Scholz*, 1972], for single-crystal quartz loaded along the *c*-axis direction

[c] Data from Figure 3 of [*Scholz*, 1972], for single-crystal quartz loaded along the *a*-axis direction. Only the average time-to-failure for 3 values of the applied stress (σ=1820, 1880 an 1920 MPa) were used for the fit.

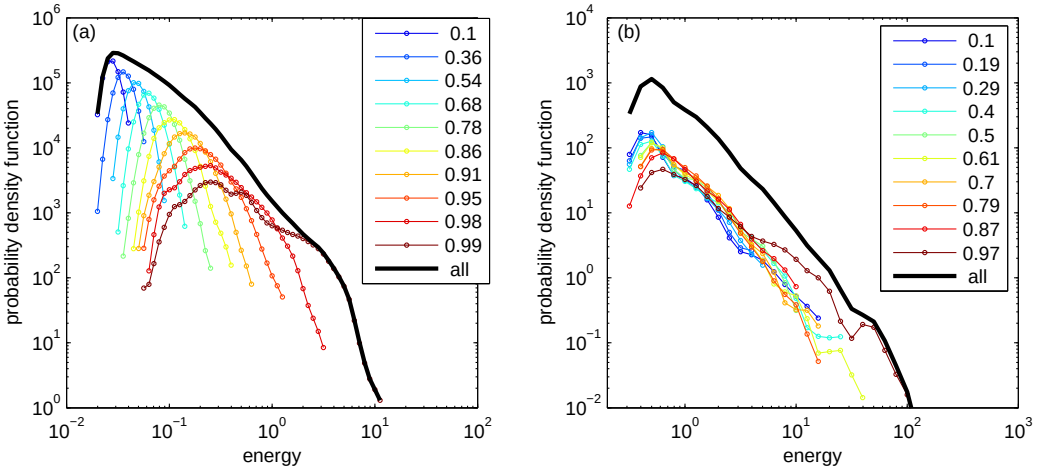

Figure 4. Energy distribution for two simulations using an exponential time-to-failure law with $b = 40$, and with time-to-failure decreasing with damage according to (12). Each plot corresponds to different values of the applied stress (a) $\sigma/\sigma_0 = 0.25$ and (b) $\sigma/\sigma_0 = 0.95$. Each colored line with dots corresponds to a different time window. Each window has the same number of events $N/10$, where the total number of events in each simulation is $N = 25283$ for $\sigma/\sigma_0 = 0.25$ and $N = 972$ for $\sigma/\sigma_0 = 0.95$. The normalized time t/t_c of the center of each window is given in the caption. The thick black line is the energy distribution for the whole simulation.

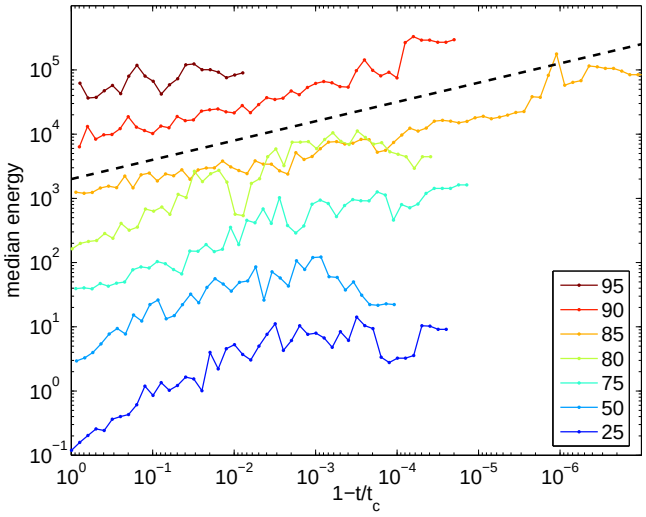

Figure 5. Typical energy release per damage event as a function of the time before failure, for different values of the applied stress (see value of σ/σ_0 in the caption), using the exponential time-to-failure law (3) with $b = 40$. We have estimated the median energy of damage events for a sliding window of 40 events. We have multiplied the median energy by an arbitrary factor for plotting purposes, the median energy at a given time t/t_c is almost independent of the applied stress. The dashed black line is a power-law with an exponent of 0.3 for reference.

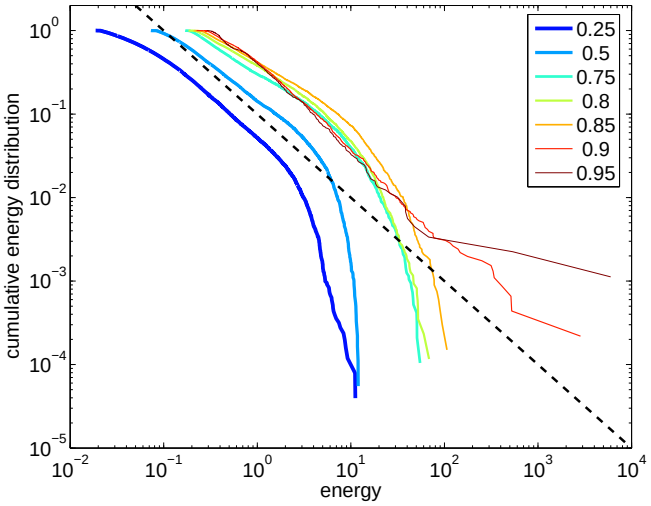

Figure 6. Cumulative energy distribution, integrated over all times, for simulations with an exponential time-to-failure law with $b = 40$, and with time-to-failure decreasing with damage according to (12). Each curve corresponds to different values of the applied stress σ/σ_0 (see caption). The dashed line shows a power-law distribution with exponent $\beta = 1$ for reference.

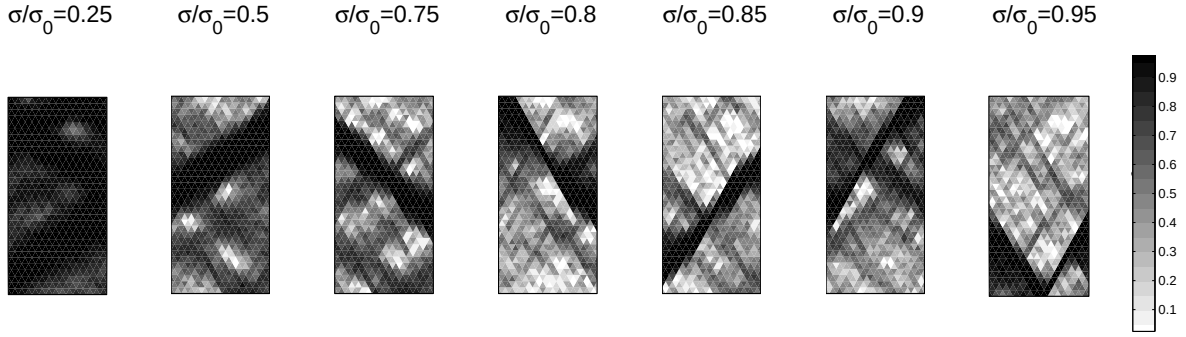

Figure 7. Damage state $D_{i,n}$ defined by (6) at the end of the simulation, for different stress values, using the power-law time-to-failure relation (4) with b'=40.

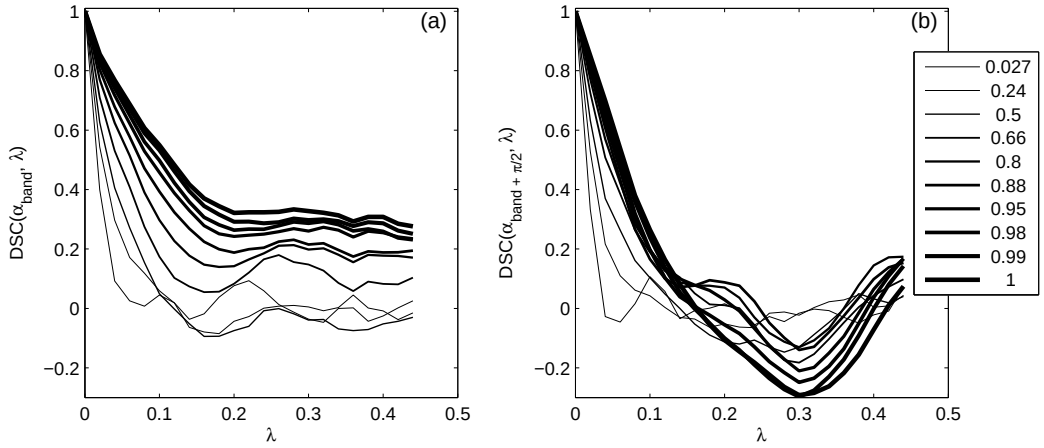

Figure 8. DSC as a function of the distance, λ, in the directions parallel (a), $\alpha_{\rm band}$, and perpendicular (b), $\alpha_{\rm band}+\pi/2$, to the damage band for successive time steps, with a step of $N/10$ between 2 curves, N being the total number of events. The legend indicates the corresponding normalized time t/t_c.

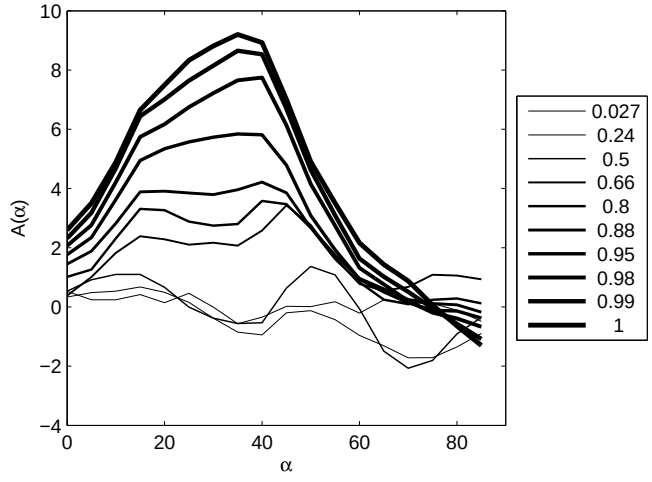

Figure 9. Coefficient of anisotropy, $A(\alpha)$ defined in (20), as a function of the direction α, for successive time steps, with a step of $N/10$ between 2 curves, N being the total number of event. The legend indicates the corresponding value of t/t_c. The applied stress is $\sigma/\sigma_0 = 0.75$. The time-to-failure is given by expression (4) with b'=40.